Inorganic Chemistry

pubs.acs.org/IC

Article

Exploring Charge Redistribution at the Cu/Co_6Se_8 Interface

Sebastian M. Krajewski, Robert J. Love, Jr., Jonathan A. Kephart, Andrew C. Boggiano, Henry S. La Pierre, Werner Kaminsky, and Alexandra Velian*

Cite This: *Inorg. Chem.* 2024, 63, 20388−20397

Read Online

ACCESS | Metrics & More | Article Recommendations | Supporting Information

ABSTRACT: This study investigates the electronic interactions and charge redistribution at the dopant−support interface using a Cu/Co_6Se_8 cluster construct. Specifically, the redox cluster series $[Cu_3Co_6Se_8L_6]^n$ ($[\mathbf{1}\text{-}Cu_3]^n$; n = 0, −1, −2, −3; L = Ph_2PNTol^-, Ph = phenyl, Tol = *p*-tolyl) spanning four distinct oxidation states is synthesized and characterized using a multitude of techniques, including multinuclear NMR, UV−vis, XANES, and X-ray crystallography. Structural investigations indicate that the clusters are isostructural and chiral, adopting a pseudo-D_3 symmetry. Paramagnetic ^{31}P NMR spectroscopy and solution-phase magnetic measurements together with DFT calculations are employed to interrogate the electronic structure and spin-state changes across the $[\mathbf{1}\text{-}Cu_3]^{3-}$ to **1**-Cu_3 redox series, revealing that the copper edge sites retain a +1 oxidation state while the Co/Se core becomes increasingly oxidized, yielding a highly zwitterionic cluster.

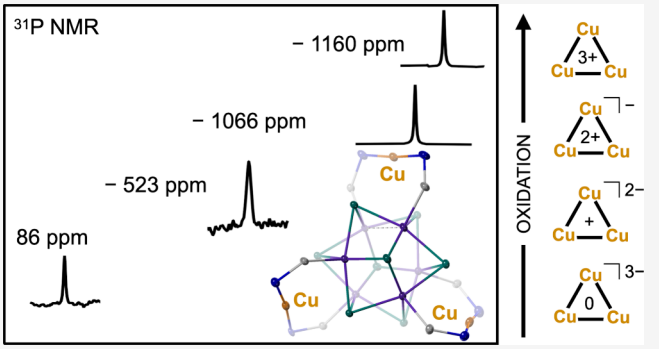

INTRODUCTION

Redox-active dopants can dramatically impact the catalytic activity of transition metal chalcogenide materials, but a detailed, atomic-level understanding of how the structural and electronic interactions at the dopant/host interface modulate reactivity remains elusive.[1−3] For example, introducing Cu(II) centers in MoS_2 materials stunts hydrodesulfurization and has little impact on hydrogen evolution, whereas Co(II) or Ni(II) improves both.[2,3] This promoter/inhibitor effect of the dopants (M) is still not completely understood and has been correlated with the ability of the dopants to reduce or oxidize the molybdenum, or to modify the strength of the M—S bonds, the morphology of the catalyst, the reactivity of sulfur active sites, and the substrate chemisorption energies.[2−5] In contrast to the structurally complex M−Mo-S materials, transition metal chalcogenide molecular clusters can be prepared with precise and uniform structures and compositions, offering the potential to investigate specific motifs found within heterogeneous catalysts.[6−17]

Our group introduced a family of transition metal chalcogenide clusters that bear resemblance to edge-decorated active sites of M−Mo-S catalysts[18] and ternary M/Mo_6S_8 Chevrel phases,[19] and that contain well-defined active sites.[3] Specifically, nanoclusters $M_3Co_6Se_8L_6$ (**1**-M_3; M = Cr, Fe, Co, Zn, Me_2Sn; L = Ph_2PNTol^-) and $MCo_6Se_8(PEt_3)_4L_2$ (**2**-M, M = Cr−Co, Cu, Zn) contain low-coordinate edge site "dopants" (M), which can double as active sites, anchored on a redox-active, diamagnetic $[Co_6Se_8]$ cluster "support" (Figure 1).[8,20−25] These structurally modular, catalytically active clusters enabled us to pursue systematic structure/function studies to map the role of metal/support interactions and interactive site (allosteric) interactions in catalysis. Mapping charge redistribution across multiple metals, particularly in response to chemical events, remains a topic of intense investigation in the molecular cluster community.[26−30] The M/Co_6Se_8 interface in our clusters is unique as it enables probing charge redistribution between a metal dopant and the support unit and its impact on catalysis. Prior investigations have revealed the presence of distinct regimes of metal/support cooperativity.[10,23,31] For instance, in a redox-independent regime, holes are localized exclusively on the edge site during an oxidative reaction. This is the case in $CrCo_6Se_8(PEt_3)_4L_2$ (**2**-Cr) where Cr(II) is significantly more reducing than the Co/Se cluster.[10] In contrast, in a redox cooperative regime, the edge and $[Co_6Se_8]$ cluster have similar reducing powers and good orbital overlap. The edge metal and the $[Co_6Se_8]$ cluster can therefore share the burden of oxidation, as in $CoCo_6Se_8(PEt_3)_4L_2$ (**2**-Co).[10] Spontaneous charge transfer can also occur between the edge and the support. For example, the single-edge cluster $CuCo_6Se_8(PEt_3)_4L_2$ (**2**-Cu) is synthesized from a Cu(II) source and a neutral Co_6Se_8 cluster, and yet **2**-Cu is best described as a Cu(I) edge installed on a mono-oxidized $[Co_6Se_8]^+$ unit.[10]

Received: June 26, 2024
Revised: October 4, 2024
Accepted: October 9, 2024
Published: October 21, 2024

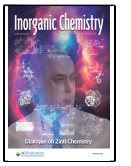

https://doi.org/10.1021/acs.inorgchem.4c02639
Inorg. Chem. 2024, 63, 20388−20397

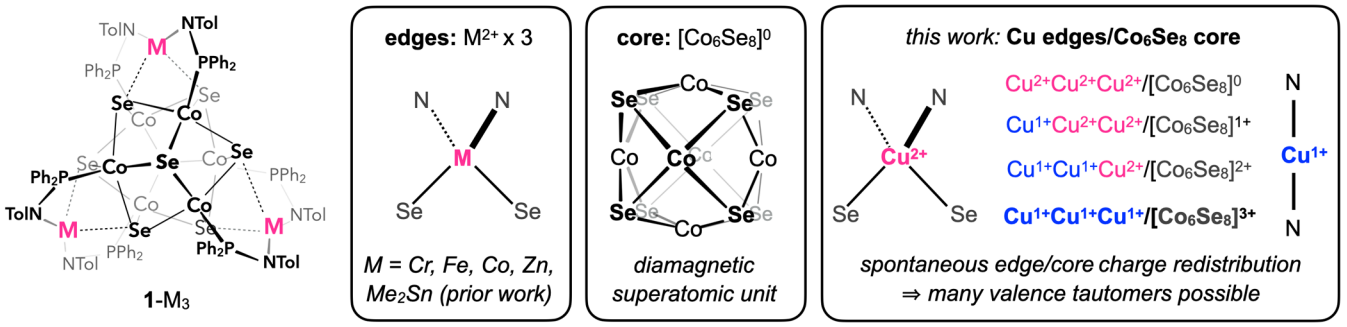

Figure 1. Ternary nanoclusters **1**-M_3 feature three edge sites (M^{2+}) anchored on a diamagnetic cluster core $[Co_6Se_8]^0$. Spontaneous edge/core electron transfer occurs when Cu^{2+} edge sites are installed.

Here, the limits of the spontaneous charge redistribution at the metal/support interface of a molecular cluster are tested by increasing the number of Cu centers on the $[Co_6Se_8]$ unit from one to three. The presence of multiple edge sites in a putative tricopper cluster could have interesting electronic consequences (Figure 1). Two scenarios are envisioned, which could coexist via valence tautomerism.[32−34] In the first, three electron transfer events occur to produce a tricopper cluster in which three Cu(I) edge sites are installed on the elusive trioxidized $[Co_6Se_8]^{3+}$ unit.[8,20,35] The second scenario would illustrate a redox allostery of the edge sites,[23,24] producing a mixture of Cu(I)/Cu(II) edge sites anchored on an oxidized $[Co_6Se_8]^n$ unit (n = +1, + 2). Our findings suggest that the former scenario is favored, and no clear evidence of valence tautomerism is observed across a wide window of redox states.

RESULTS AND DISCUSSION

Treatment of the hexalithiated salt $Li_6(py)_6Co_6Se_8L_6$ (**1**-$Li_6(py)_6$; py = pyridine) with copper(I) bromide dimethyl sulfide (6.1 equiv) produces a single, paramagnetic cluster over the course of 16 h. This compound is isolated as a dark brown crystalline solid following a standard solvent workup (Scheme 1a). In solution, the product is symmetrical and contains no bound solvent. NMR spectroscopy analysis reveals a single ^{1}H environment for the amidophosphine ligand and a broad ^{31}P peak at −1065 ppm ($\nu_{1/2}$ = 1180 Hz), indicative of paramagnetism (Figures S8 and S9).

Scheme 1. Synthesis of $[Li(thf)_4][1\text{-}Cu_3]$ and $[Li(thf)_4]_2[1\text{-}Cu_3]$

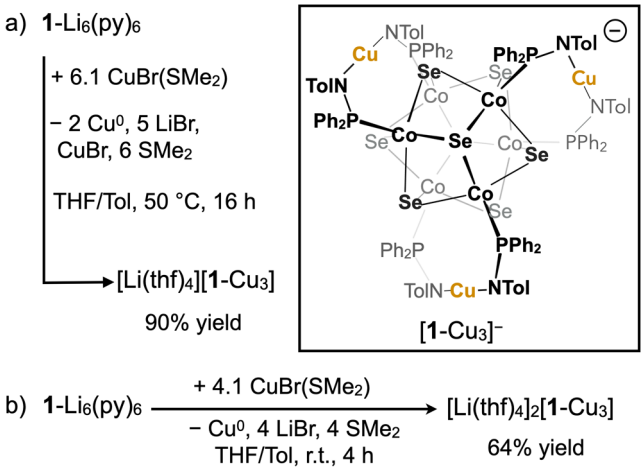

Single-crystal X-ray diffraction analysis identified this species as the tricopper cluster salt $[Li(thf)_4][1\text{-}Cu_3]$ (thf = tetrahydrofuran), where each of the three edge sites is occupied by a single copper atom free of bound exogeneous ligands. The linear N−Cu−N geometry (Figure 2b, Table S3) is suggestive of a +1 oxidation state.[10,36] Formally, the anionic cluster $[1\text{-}Cu_3]^-$ contains three Cu(I) edge sites anchored on a doubly oxidized $[Co_6Se_8]^{2+}$ cluster core. Given the relatively weak oxidizing capability of copper(I), we propose that the starting material disproportionates in situ upon heating and forms multiple equivalents of copper(II), which is able to oxidize the $[Co_6Se_8]^0$ cluster core twice.[37,38]

If the **1**-$Li_6(py)_6$ cluster is treated instead with four equivalents of $CuBr(SMe_2)$ and kept at room temperature during the reaction, the cluster core is only oxidized once during transmetalation, yielding the dianionic salt $[Li(thf)_4]_2[1\text{-}Cu_3]$ (Scheme 1b). The independent synthesis of $[1\text{-}Cu_3]^{2-}$ by the reduction of $[1\text{-}Cu_3]^-$ is discussed in a later section. Treatment of **1**-$Li_6(py)_6$ with copper(II) chloride (3 equiv) does not produce a tricopper cluster, instead leading to complex reactivity beyond the scope of this work.

The monoanionic tricopper(I) cluster $[1\text{-}Cu_3]^-$ has no observable affinity for exogenous ligands (e.g., THF, py, and CO; SI 1.1), and in contrast to other **1**-M_3 clusters, it does not undergo hydrolysis in the presence of water (3 M in CH_3CN, 24 h, room temperature). The increased stability and low reactivity of linear Cu(I) bisamides are documented and have been attributed to the strong σ-donating ability of the supporting ligands and the high covalency of the Cu−N bonds.[39−41] Solid-state analysis of $[1\text{-}Cu_3]^-$ reveals that the Cu−N distances (1.90(1) Å avg.) are consistent with the average bond reported in the CCDC database of 2.0(1) Å[42] and those in the monometalated cluster **2**-Cu of 1.893(4) Å.[10]

Cu/$[Co_6Se_8]$ Redox Series. The electronic structure of the cluster is probed chemically and electrochemically. Cyclic voltammetry analysis of $[1\text{-}Cu_3]^-$ indicates three quasireversible, single-electron events: two reductions and one oxidation at −1.33, −0.72, and −0.02 V vs $Fc^{+/0}$, respectively (Figures 3a and S15). The large separation between these redox events indicates that all the individual members of the $[1\text{-}Cu_3]^n$ (n = 0 to −3) series might be stable toward isolation. Indeed, chemical one- and two-electron reductions, as well as one-electron oxidation of $[1\text{-}Cu_3]^-$ are successfully accomplished using reagents of appropriate redox strength (Scheme 2).[38] One-electron reduction of $[1\text{-}Cu_3]^-$ with $CoCp_2$ (Cp = C_5H_5; 1 equiv) yields the $[CoCp_2][Li(thf)_4][1\text{-}Cu_3]$ salt, and two-electron reduction with $CoCp^*_2$ (Cp* = C_5Me_5; 2 equiv) produces $[CoCp^*_2]_2[Li(thf)_4][1\text{-}Cu_3]$. The dianionic cluster

https://doi.org/10.1021/acs.inorgchem.4c02639
Inorg. Chem. 2024, 63, 20388−20397

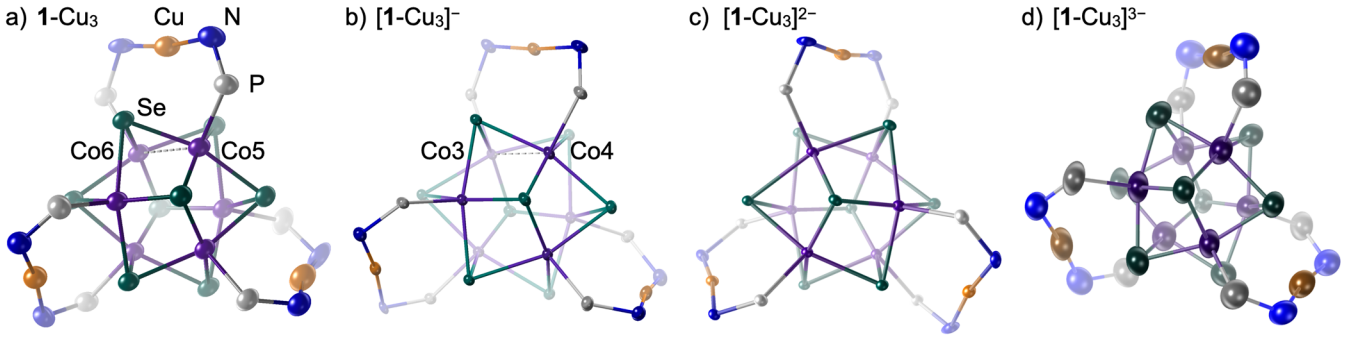

Figure 2. Comparison of the single-crystal solid-state structures of (a) **1**-Cu_3, (b) $[Li(thf)_4][\mathbf{1}\text{-}Cu_3]$, (c) $[Ru(bpy)_3][\mathbf{1}\text{-}Cu_3]$, and (d) $[CoCp^*_2]_2[Li(thf)_4][\mathbf{1}\text{-}Cu_3]$, with organic ligands and cations truncated for clarity. Thermal ellipsoids are drawn at the 50% probability level.

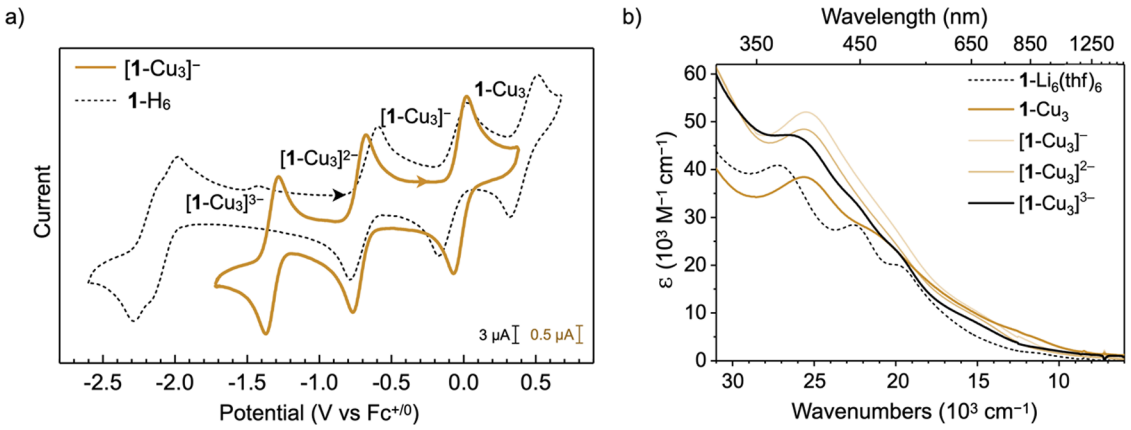

Figure 3. (a) Cyclic voltammograms of **1**-H_6 and $[Li(thf)_4][\mathbf{1}\text{-}Cu_3]$ (0.1 M $TBAPF_6$ in THF, at scan rates of 200 and 25 mV/s, respectively, currents are normalized). (b) UV−vis−NIR absorption spectra of $[\mathbf{1}\text{-}Li_6(thf)_6]$, **1**-$Cu_3$, $[Li(thf)_4][\mathbf{1}\text{-}Cu_3]$, $[Li(thf)_4]_2[\mathbf{1}\text{-}Cu_3]$, and $[CoCp^*_2]_2[Li(thf)_4][\mathbf{1}\text{-}Cu_3]$ acquired in THF.

Scheme 2. (a) Synthesis of the Redox Series $[\mathbf{1}\text{-}Cu_3]^n$, n = 0, −2, −3 via Chemical Oxidation and Reduction of $[\mathbf{1}\text{-}Cu_3]^-$, and (b) Proposed Oxidation State of the Co/Se Cluster Core within the Redox Series

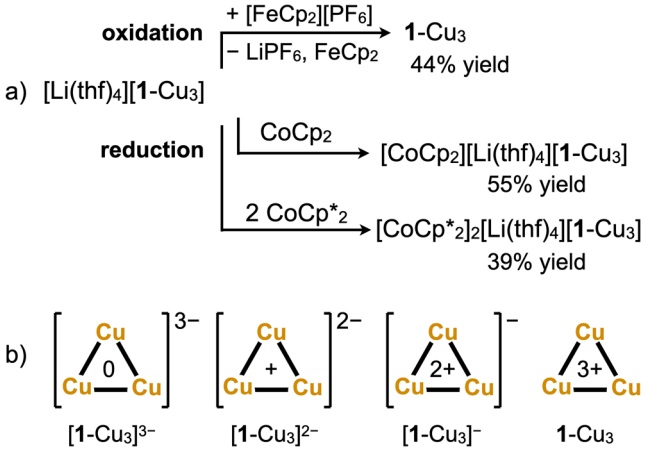

$[\mathbf{1}\text{-}Cu_3]^{2-}$ has also been isolated as the $[Ru(bpy)_3][\mathbf{1}\text{-}Cu_3]$ (bpy = 2,2′-bipyridine; SI 1.2 and Figure 2c) salt following cation exchange. Cyclic voltammetry reveals that the trianionic cluster $[\mathbf{1}\text{-}Cu_3]^{3-}$ is significantly more reducing than the isoelectronic **1**-H_6 cluster, ostensibly due to the presence of the anionic copper-bisamido unit edge sites (Figure 3a).[43]

In contrast to chemical reduction, the success of chemical mono-oxidation of $[\mathbf{1}\text{-}Cu_3]^-$ is strongly dependent on the coordinating ability of the solvent and the identity of the counterion. While one-electron oxidation with $[FeCp_2][PF_6]$ (1.0 equiv) occurs readily in THF to produce the neutral cluster **1**-Cu_3, no reaction occurs in CH_2Cl_2 even with strong oxidizing agents such as $AgPF_6$, $[N(C_6H_4Br\text{-}4)_3][SbCl_6]$, or WCl_6.[38] Meanwhile, one-electron oxidation of $[TBA][\mathbf{1}\text{-}Cu_3]$, obtained via cation exchange from $[Li(thf)_4][\mathbf{1}\text{-}Cu_3]$ and [TBA]Cl, with $[FeCp_2][PF_6]$ proceeds with or without a coordinating ligand present (Section S1.3). We attribute this solvent dependence to the association of the lithium cation with the cluster. Indeed, NMR analysis indicates that the symmetry of the $[Li(thf)_4][\mathbf{1}\text{-}Cu_3]$ cluster lowers dramatically when dissolved in noncoordinating solvents (i.e., C_6D_6 and CD_2Cl_2), suggesting ion association. In benzene-d_6, three distinct amidophosphine ligand environments are observable by ^1H and ^{31}P NMR spectroscopy. Two lithium signals are detected by ^7Li NMR spectroscopy—one at 0.4 ppm, attributed to a $Li(thf)_4^+$ ion, and another broad peak at 16.7 ppm ($\nu_{1/2}$ = 200 Hz), attributed to $Li(thf)_x^+$ ions associated with the paramagnetic cluster core, likely at N or Se sites (Figures S9−S12). We hypothesize that ion pairing with the Lewis-acidic lithium cation depletes the cluster of electron density, making it more resistant to oxidation.

$[\mathbf{1}\text{-}Cu_3]^n$ are strong absorbers and have UV−vis−NIR spectral profiles characteristic of **1**-M_3 and **1**-$Li_6(thf)_6$ clusters. As illustrated in Figure 3b, all the clusters have a main feature with λ_{max} (ε) ranging from 389 nm (36,000 $M^{-1}cm^{-1}$) for $[Li(thf)_4][\mathbf{1}\text{-}Cu_3]$ to 392 nm (50,000 $M^{-1}cm^{-1}$) for $[Li(thf)_4][Cp_2Co][\mathbf{1}\text{-}Cu_3]$ and absorption tails that extend into

https://doi.org/10.1021/acs.inorgchem.4c02639
Inorg. Chem. 2024, 63, 20388−20397

near-IR. The absorption in the near-IR region redshifts as electrons are removed from the system, with the lowest energy values for **1**-Cu_3. However, the significance of this trend in connection to the possible observation of intervalence charge transfer bands is currently not well understood (Figure 3b).

With three Cu(I) edge sites and a trioxidized Co/Se core, **1**-Cu_3 represents the first reported example of a $[Co_6Se_8]^{3+}$ cluster. In agreement with this oxidation state assignment, electron paramagnetic resonance spectroscopy of **1**-Cu_3 at 100 K does not indicate the presence of Cu(II) (Figure S27). **1**-Cu_3 is resistant to further oxidation, highlighting the difficulty of directly oxidizing the Cu(I) sites to Cu(II) in this system. It also suggests that the tetraoxidized form of the Co/Se core is not synthetically accessible with standard reagents. Valence tautomerization is not identified in **1**-Cu_3. For instance, **1**-Cu_3 is thermally stable (24 h, 80 °C) and does not convert to a new species (e.g., **1**-$Cu^{II}Cu^{I}_2$) even in the presence of coordinating ligands (THF, py, PMe_3, ^{t}BuCN, and CO). The reorganization energy cost associated with this putative inner-sphere electron transfer that would oversee a linear Cu(I) convert to a pseudotetrahedral or square planar Cu(II) center could be prohibitive,[39] whereas there is minimal entropic cost associated with the oxidation or reduction of the Co_6Se_8 core. A limited number of two-coordinate linear copper(II) amido complexes are known, but they are not synthesized through the oxidation of a linear copper(I) complex.[44−46]

Isostructurality and Helical Chirality across the Redox Series. The solid-state structures of the tricopper cluster redox series $[\mathbf{1}\text{-}Cu_3]^n$ (n = 0, −1, −2, −3) are obtained using single-crystal X-ray diffraction analysis (Figure 2). While the data sets for **1**-Cu_3, $[Li(thf)_4][\mathbf{1}\text{-}Cu_3]$, and $[Ru(bpy)_3][\mathbf{1}\text{-}Cu_3]$ are sufficiently high quality to enable a bond metric comparison, the crystal structure of $[CoCp^*_2]_2[Li(thf)_4][\mathbf{1}\text{-}Cu_3]$ is fraught with extensive cation and solvent disorder, precluding a bond metric discussion. The Cu/Co/Se clusters retain the pseudo-D_3 symmetry across the redox series. The copper(I) amidophosphine units remain relatively rigid and nearly linear, with ∠NCuN angles ranging from 168.0(3) to 175.0(3)°, and an average Cu···Se distance of 2.80 Å, indicating that no binding interaction is present (Table S3).[47]

A bond metric comparison informs on the distribution of electron density between the copper edge sites and the Co/Se core, lending support to the proposal that while copper maintains a +1 oxidation state, $[Co_6Se_8]$ is the locus of redox-state changes, ranging from +3 in **1**-Cu_3 to neutral in $[\mathbf{1}\text{-}Cu_3]^{3-}$. Although the Co−Se, Cu···Se, and Cu−N interatomic distances do not vary significantly with oxidation-state changes, the Co···Co and Co−P interatomic distances are informative (Figure 4; Table S3). A basic molecular diagram of the Co_6Se_8 cluster core[48] predicts that as electrons are removed from it, antibonding Co···Co orbitals are depopulated and the Co···Co bonding character increases. Indeed, a contraction in the Co···Co distances in the Co/Se core has been empirically associated with oxidation.[20,49] Figure 4 reflects this trend: as one, two, and three electrons are removed from the Co/Se cluster, the Co···Co average distances contract from 2.946(7) Å in the neutral Co_6Se_8 core of **1**-H_6 to 2.85(2) Å in **1**-Cu_3 and $[\mathbf{1}\text{-}Cu_3]^-$. In fact, **1**-$Cu_3$ and $[\mathbf{1}\text{-}Cu_3]^-$ feature one short Co···Co distance of 2.683(3) and 2.682(2) Å, respectively, consistent with a weak Co−Co bonding interaction.[50] Density functional theory calculations indicate Mayer bond orders of 0.44 and 0.12 for the Co/Co pairs with short and long contacts in $[\mathbf{1}\text{-}Cu_3]^-$, respectively.[51] The average Co−P distances in the redox series oppose the trend of the Co···Co distances, increasing with the oxidation of the Co/Se core from 2.129(1) Å (average) in **1**-H_6 to 2.162(5) Å in $[\mathbf{1}\text{-}Cu_3]^{2-}$ to 2.196(1) Å in **1**-Cu_3. As electrons are removed from the Co_6Se_8 cluster, the cobalt atoms participate in weaker back-bonding with the phosphines.[52]

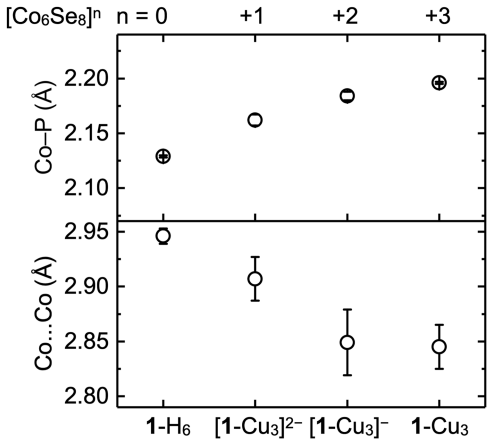

Figure 4. Comparison of average bonding parameters obtained via crystallography as a function of the cluster core oxidation state. Error bars represent the standard error for each set of crystallographic distances.

The propeller-like arrangement of the copper−amidophosphine units on the surface of the Co/Se core results in inherent helical chirality.[53] While all **1**-M_3 clusters are helically chiral, $[Li(thf)_4][\mathbf{1}\text{-}Cu_3]$ is the first to form enantiomerically pure single crystals. The presence of individual single crystals of single-handedness is confirmed experimentally by X-ray crystallography; $[Li(thf)_4][\mathbf{1}\text{-}Cu_3]$ crystallizes in the chiral space group $P2_12_12_1$. This spontaneous chiral resolution by crystallization is a relatively rare phenomenon,[54] and is being explored as a pathway to isolate chiral cluster samples at scale.

Solution Magnetism and Paramagnetic ^{31}P NMR Studies To Elucidate Spin-State Changes in the Redox Series. Solution magnetic susceptibility measurements of $[Li(thf)_4][\mathbf{1}\text{-}Cu_3]$ using Evans' method[55] produce an overall magnetic moment of 2.1 Bohr magnetons, intermediate to the expected spin-only magnetic moment values of 1.73 and 2.83 Bohr magnetons for the spin states of S = 1/2 and 1, respectively. The $[\mathbf{1}\text{-}Cu_3]^-$ cluster has an even number of electrons and therefore would nominally be expected to have either a closed shell or a triplet ground state (S = 0 or 1). Meanwhile, Evans' method measurements for $[Li(thf)_4]_2[\mathbf{1}\text{-}Cu_3]$ and **1**-Cu_3 result in effective magnetic moments of 1.6 Bohr magnetons, which are consistent with an S = 1/2 spin state. Molecular orbital theory predicts that the HOMO in a Co_6Se_8 system is triply degenerate,[48] and DFT calculations on the homoleptic cluster $Co_6Se_8(PEt_3)_6$ similarly predict a doubly degenerate HOMO level followed closely by the HOMO−1 only 0.02 eV lower in energy.[43] Both situations would theoretically yield a $[Co_6Se_8]^{2+}$ cluster core in the S = 1 state.

^{31}P NMR spectroscopy analysis of the redox series $[\mathbf{1}\text{-}Cu_3]^n$ (n = 0, −1, −2, −3) indicates that all four compounds remain nominally D_3 symmetric in coordinating solvents. While ^{1}H NMR chemical shifts are relatively unremarkable and span the diamagnetic window, the ^{31}P nuclei serve as diagnostic reporters on the electronic state of the clusters,[10] featuring

https://doi.org/10.1021/acs.inorgchem.4c02639
Inorg. Chem. 2024, 63, 20388−20397

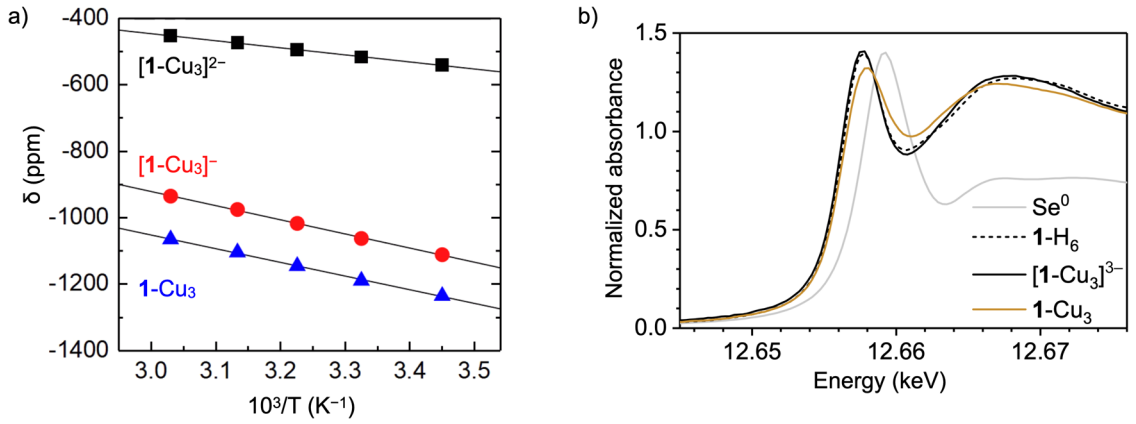

Figure 5. (a) Curie behavior of $[\mathbf{1}\text{-}Cu_3]^n$ (n = 0, −1, −2) reflected in the linear dependence of the ^{31}P NMR shifts with the inverse of temperature (290−330 K). (b) Se XANES spectra of $\mathbf{1}\text{-}Cu_3$, $[CoCp^*_2]_2[Li(THF)_4][\mathbf{1}\text{-}Cu_3]$, $\mathbf{1}\text{-}H_6$, and Se foil. The signal for the Se foil is scaled to enable comparison to the clusters.

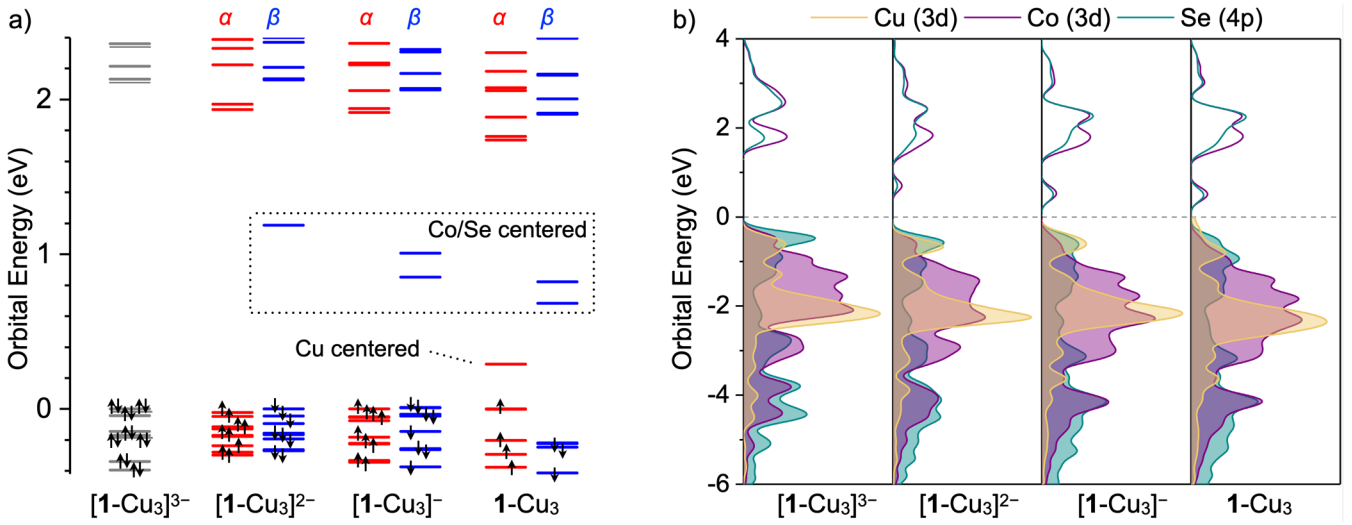

Figure 6. (a) Molecular orbital diagrams for $[\mathbf{1}\text{-}Cu_3]^n$ (n = 0, −1, −2, −3) calculated at the B3LYP+/ccPVTZ level of theory. Alpha (α) and beta (β orbitals for the open-shell clusters are colored red and blue, respectively, and (b) corresponding partial density of states plots. To facilitate comparisons, each top-occupied orbital is normalized to a value of 0 eV.

chemical shifts that undergo dramatic changes with the redox state. The ^{31}P NMR chemical shifts range from 80 ppm for the diamagnetic $[\mathbf{1}\text{-}Cu_3]^{3-}$ to −1160 ppm in $\mathbf{1}\text{-}Cu_3$ (Figure 5). As expected, the paramagnetic centers greatly reduce the relaxation times of the ^{31}P signals, from 162(2) ms in $\mathbf{1}\text{-}H_6$ to 1.6(1)—3.4(1) ms in $[\mathbf{1}\text{-}Cu_3]^n$, n = 0, −1, −2 (Figures S28−S31).

Paramagnetic NMR chemical shifts (δ_T^{obs}) are a result of diamagnetic (δ^{dia}) and paramagnetic contributions (δ^{para}), as described by eq S1.[56] Since δ^{para} depends on the total spin and temperature, variable-temperature ^{31}P NMR measurements can inform on the electronic structure of the compounds measured. Plotting the ^{31}P NMR chemical shifts of $[\mathbf{1}\text{-}Cu_3]^n$ (n = 0, −1, −2) vs the inverse of temperature (T = 290−330 K; Figure 5a and Table S1) confirms a linear Curie−Weiss relationship and rules out any unexpected behavior of the clusters such as ferromagnetism.[57] The temperature-independent ^{31}P NMR chemical shifts (δ^{TIP}) can further inform on the spin state of the clusters. These originate from temperature-independent sources of paramagnetism such as Van Vleck or Pauli susceptibilities,[57] the former of which is proportional to the number of unpaired spins.[58] In particular, Van Vleck susceptibilities have been previously observed in oxidized Co_6Te_8 clusters and could be relevant in the $[\mathbf{1}\text{-}Cu_3]^n$ series.[59,60] Here, temperature-independent chemical shifts were estimated by extrapolating the linear fits of the observed ^{31}P NMR chemical shift to an infinite temperature. The δ^{TIP} values obtained for $[\mathbf{1}\text{-}Cu_3]^{2-}$ and $\mathbf{1}\text{-}Cu_3$ are nearly equivalent, of 190(13) and 182(27) ppm, respectively, lending support to the equivalent spin state attribution of S = 1/2. Meanwhile, δ^{TIP} for $[\mathbf{1}\text{-}Cu_3]^-$ is calculated to be 354(25) ppm, nearly twice that of the other clusters, suggestive of an S = 1 spin state. The behavior of $[\mathbf{1}\text{-}Cu_3]^-$ was further probed by ^{31}P VT-NMR experiments over an extended temperature range (340−200 K). No deviations from linearity (indicative of spin crossover) were observed in this temperature window (Figure S35).[61]

X-ray Absorption Spectroscopy Probes Electronic Changes at Se. To further understand the electronic changes within the cluster core, $\mathbf{1}\text{-}H_6$, $[\mathbf{1}\text{-}Cu_3]^{3-}$, and $\mathbf{1}\text{-}Cu_3$ were analyzed via selenium K-edge X-ray absorption near-edge structure spectroscopy (XANES; Figure 5b, Table S2). The pre-edge feature (Se 1s to 4p; 12.657 keV) is similar to that seen in transition metal selenides (12.657 keV in $Cu_2Mo_6Se_8$ and 12.656 keV in CdSe)[62−64] and is consistent with a Se(−2)

https://doi.org/10.1021/acs.inorgchem.4c02639
Inorg. Chem. 2024, 63, 20388−20397

oxidation state. The pre-edge feature shifts by 0.3 eV between $[\mathbf{1}\text{-}Cu_3]^{3-}$ and $\mathbf{1}\text{-}Cu_3$, indicating a slight increase in the oxidation state of the Se sites as the Co/Se cluster undergoes a three-electron oxidation.[65] For comparison, the one-electron oxidation of the cationic cluster $[Fe_2Se_2]^{+1/+2}$ is associated with a positive shift of 0.6 eV of the pre-edge feature.[66] In this instance, the larger magnitude could be attributed to the increased variation in charge per Se atom (1 e^-/2 Fe, 2 Se) compared to the Co_6Se_8 cluster (3 e^-/6 Co, 8 Se). The Se XANES data reflect the similarity between the isoelectronic $\mathbf{1}\text{-}H_6$ and $[\mathbf{1}\text{-}Cu_3]^{3-}$ clusters, which feature neutral Co_6Se_8 cores (Figure S38).

Insights into the Electronic Structure via DFT Calculations. The electronic structure of the $[\mathbf{1}\text{-}Cu_3]^n$ (n = 0, −1, −2, −3) redox series was modeled using density functional theory (DFT; Section S5). The optimized geometries reflect experimentally observed trends in Co−P and Co···Co distances (Table S6). As expected, the closed-shell cluster $[\mathbf{1}\text{-}Cu_3]^{3-}$ features an electronic structure resembling that of $Co_6Se_8(PEt_3)_6$, with a near-triply degenerate highest occupied molecular orbital (HOMO) and a doubly degenerate lowest unoccupied molecular orbital (LUMO; Figure 6a).[43]

The frontier electronic states are plotted as molecular orbital diagrams (Figure 6a) and also as density of states plots that better illustrate elemental contributions (Figure 6b).[67] The neutral and dianionic clusters both have a singly occupied molecular orbital (SOMO) that is significantly higher in energy than the other occupied frontier orbitals, consistent with the observed S = 1/2 spin state, while the monoanionic cluster has a more ambiguous electronic structure with several pseudodegenerate orbitals at the frontier. Considering both the alpha (α) and beta (β) manifolds in $[\mathbf{1}\text{-}Cu_3]^-$, the three occupied orbitals that are highest in energy are separated by only 0.01 eV in total. Their pseudodegeneracy is possibly a consequence of the deviations from the idealized D_3 geometry in the optimized structure, which results in slight energy differences in nominally equivalent orbitals. Jahn−Teller-type distortions could be responsible for the partially quenched magnetic moment of $[\mathbf{1}\text{-}Cu_3]^-$, as observed experimentally by Evans' method.[68]

The density of states plots indicates that the copper character in the occupied frontier orbitals increases substantially as electrons are removed from $[\mathbf{1}\text{-}Cu_3]^{3-}$ until it becomes exclusively copper centered in $\mathbf{1}\text{-}Cu_3$ (Figures 6b and S47). This is aligned with our interpretation of the experimental data: as 1, 2, and 3 electrons are removed from $[\mathbf{1}\text{-}Cu_3]^{3-}$, the copper edge sites retain their +1 oxidation state, while the Co/Se core becomes increasingly oxidized. Indeed, even in the highly oxidized cluster $\mathbf{1}\text{-}Cu_3$, there is little contribution from copper to the unoccupied electronic states. Correspondingly, the LUMO and LUMO+1 orbitals are localized on the Co/Se core for all members of the redox series, consistent with experimental results suggesting core-based oxidation.[10] Additionally, as the cluster increases in the oxidation state, the selenium character of the occupied frontier states gradually diminishes. We attribute this to the partial oxidation of Se, in line with the Se XANES data discussed above.

CONCLUSIONS

Atomically precise and entropically robust, the $[\mathbf{1}\text{-}Cu_3]^n$ (n = 0, −1, −2, −3) clusters enable detailed mapping of the structural and electronic interactions at the Cu/Co_6Se_8 dopant/support interface. Experimental and DFT investigations suggest that as electrons are removed from the $[\mathbf{1}\text{-}Cu_3]^{3-}$ cluster, the copper edge sites retain a + 1 oxidation state while the Co/Se core becomes increasingly oxidized. The series culminates with the formation of $\mathbf{1}\text{-}Cu_3$, a highly zwitterionic species with three Cu(I) edge sites anchored but not binding directly to the triply oxidized $[Co_6Se_8]^{3+}$ core. The reluctance of the copper(I) edge sites to undergo oxidation and the absence of any apparent valence tautomerism may be attributed to the large entropic cost of entering a tetracoordinate coordination geometry favorable to copper(II).

EXPERIMENTAL SECTION

General Information. All syntheses were conducted under a dinitrogen atmosphere using a standard Schlenk line or an LC Technology Solutions glove box equipped with a freezer set to −35 °C. All glassware was dried at 160 °C for a minimum of 12 h prior to use. Additional experimental and computational details, materials, and methods can be found in the Supporting Information file (PDF) and the optimized coordinates file (xyz).

Computational Methods. All DFT calculations were performed using Gaussian 16, Revision A.03 quantum chemistry program package for the Linux operating system.[69] The initial starting point geometries were obtained by using the crystallographically obtained structure of $[Li(thf)_4][\mathbf{1}\text{-}Cu_3]$ as a starting point and optimizing to a minimum, followed by analytical frequency calculations (Hessian) to confirm that no imaginary frequencies were present. Prior to optimization, the cation was omitted from the structure, and the methyl groups on the tolyl groups of the aminophosphine ligands were replaced with hydrogen atoms to reduce the computation time. The geometry optimizations were performed using unrestricted DFT calculations (except for $[\mathbf{1}\text{-}Cu_3]^{3-}$, which was restricted) at a pure GGA functional level using Becke's 1988 gradient-corrected exchange functional and Perdew's 1986 electron correlation functional (uBPV86) and def2SVP basis set. The optimized geometry of the $[\mathbf{1}\text{-}Cu_3]^-$ anion was used as the starting point for the optimization of the other clusters in the series. Using the optimized geometries, single-point calculations were performed at uB3LYP+/cc-pVTZ that were used for orbital energy diagrams and spin density calculations. Doublet spin states were assumed for $[\mathbf{1}\text{-}Cu_3]^{2-}$ and $\mathbf{1}\text{-}Cu_3$, while $[\mathbf{1}\text{-}Cu_3]^-$ was modeled as a triplet. Multiwfn was used to generate partial density of states plots and calculate Mayer bond orders.[67] This level of theory and approach have been previously utilized to reproduce defining experimental features of the $\mathbf{1}\text{-}M_3$ and 2-M clusters.[10,25]

Synthetic Procedures. *Synthesis of [Li(thf)$_4$][1-Cu$_3$].* Inside the glove box, a 200 mL Schlenk flask with a Teflon-coated stir bar was charged with $\mathbf{1}\text{-}Li_6(py)_6$ (5.500 g, 1.7 mmol) and copper(I) bromide dimethylsulfide (2.127 g, 10.3 mmol). Toluene (70 mL) and tetrahydrofuran (25 mL) are added to the flask, resulting in a dark brown solution upon mixing. The flask is capped with a rubber septum and heated in an oil bath to 50 °C for 16 h. The flask is cooled and returned to the glove box, and the solvent is removed from the reaction mixture under reduced pressure. The dark brown residue was dissolved in minimal tetrahydrofuran, combined with toluene (50 mL) and pentane (50 mL), and left to sit at room temperature for 12 h. The resulting crystals are isolated by vacuum filtration over a medium-pore frit and washed with toluene (50 mL) and pentane (30 mL). The product is obtained as a black crystalline solid after the volatiles are removed in vacuo (4.770 g, 1.58 mmol, 87%). The compound can be handled in air and does not hydrolyze if treated with water in acetonitrile at 25 °C (3 M) for a period of at least 12 h. ^{1}H NMR (acetonitrile-d_3, 500 MHz) δ: 8.74 (s, 6H, -Ph), 8.31 (d, J = 7.4 Hz, 12H, -Ph), 7.35 (t, J = 7.3 Hz, 6H, -Ph), 7.04 (t, J = 7.4 Hz, 12H, -Ph), 6.72−6.66 (d, J = 7.4 Hz, 12H, -C_6H_4-p-Me), 6.58 (d, J = 7.8 Hz, 24 Hz, -Ph), 5.04 (d, J = 7.3 Hz, 12H, -C_6H_4-p-Me), 1.99 (s, 18H, -CH_3). ^{31}P NMR (acetonitrile-d_3, 283 MHz) δ: −1065.8 ($\nu_{1/2}$ = 1200 Hz, T_1 = 3.4 ms). ^{31}P NMR (benzene-d_6, 283 MHz) δ: −960.9 ($\nu_{1/2}$ = 900 Hz), −990.8 ($\nu_{1/2}$ = 650 Hz), −1033.2 ($\nu_{1/2}$ = 2000 Hz). ^{7}Li NMR (acetonitrile-d_3, 194 MHz) δ: −2.45 ($\nu_{1/2}$ = 18

https://doi.org/10.1021/acs.inorgchem.4c02639
Inorg. Chem. 2024, 63, 20388−20397

Hz). ^{7}Li NMR (benzene-d_6, 194 MHz) δ: 16.68 ($\nu_{1/2}$ = 180 Hz), 0.38 ($\nu_{1/2}$ = 45 Hz). ^{13}C NMR (acetonitrile-d_3, 126 MHz) δ: 134.42, 133.17, 131.78, 131.66, 128.56, 125.77, 124.83, 124.80, 121.25, 120.93, 20.70. μ_{eff} (Evan's method, CD_3CN, 298 K): 2.06 μ_B. UV−vis (acetonitrile): λ_{max} (ε) 389 nm (36,000 $M^{-1}cm^{-1}$). Elemental analysis (ICP−MS): experimental (calculated for $C_{130}H_{134}Co_6Cu_3LiN_6O_4P_6Se_8$) Co 11.00 (11.11) Se 19.90 (19.66) P 5.82 (5.78).

Synthesis of [Li(thf)$_4$][Cp$_2$Co][1-Cu$_3$]. Inside the glove box, a 100 mL round-bottomed flask is charged with [Li(thf)$_4$][**1**-Cu$_3$] (0.622 g, 0.19 mmol) and a Teflon-coated stir bar. Tetrahydrofuran (30 mL) is added to the flask, and the mixture is stirred until a homogeneous solution is formed. Cobaltocene (0.038 g, 0.20 mmol) is weighed out into a vial and dissolved in tetrahydrofuran (10 mL), and the solution is added to the flask while stirring. Within a few minutes, a dark brown precipitate forms. After stirring for 12 h, the precipitate is isolated via vacuum filtration over a medium-pore frit and washed with diethyl ether (50 mL). After removing volatiles under reduced pressure, the product is obtained as a black, spectroscopically pure powder (0.360 g, 0.106 mmol, 55%). ^{1}H NMR (acetonitrile-d_3, 500 MHz) δ: 8.12−8.06 (m, 18H, -Ph), 7.62 (s, 6H, -Ph), 7.18 (s, 12H, -Ph), 6.91 (s, 12H), 6.79 (s, 12H, -Ph), 6.21 (s, 12H, -C$_6H_4$-p-Me), 6.12 (s, 12H, -C$_6H_4$-p-Me), 5.63 (s, Cp), 1.78 (s, 18H,-Me). ^{31}P NMR (acetonitrile-d_3, 283 MHz) δ: −522.6 ($\nu_{1/2}$ = 3600 Hz). ^{7}Li NMR (acetonitrile-d_3, 194 MHz) δ: −2.47 ($\nu_{1/2}$ = 10 Hz). μ_{eff} (Evan's method, CD_3CN, 298 K): 1.65 μ_B. UV−vis (acetonitrile): λ_{max} (ε) 392 nm (50,000 M^{-1} cm^{-1}). Elemental analysis (ICP−MS): experimental (calculated for $C_{140}H_{144}Co_7Cu_3LiN_6O_4P_6Se_8$) Co 10.31 (12.12) Se 18.70 (18.57) P 5.36 (5.46).

Synthesis of [Li(CH$_3$CN)$_4$][Cp$_2$Co]$_2$[1-Cu$_3$].* Inside the glove box, [Li(thf)$_4$][**1**-Cu$_3$] (0.350 g, 0.11 mmol) is weighed out into a vial equipped with a Teflon-coated stir bar and dissolved in acetonitrile (10 mL). Decamethylcobaltocene (0.072 g, 0.22 mmol) is weighed out into a separate vial and added directly to the flask, resulting in a color change of the solution to dark red−brown. After stirring for 12 h, the solution is concentrated to half the initial volume and mixed with diethyl ether (30 mL). The resulting precipitate is isolated by vacuum filtration over a medium-pore frit and washed with diethyl ether (30 mL). After removing volatiles under reduced pressure, the product is obtained as a black powder (0.162 g, 0.042 mmol, 39%). The product is unstable toward halogenated solvents such as dichloromethane. ^{1}H NMR (acetonitrile-d_3, 500 MHz) δ: 7.55−7.04 (m 66H), 6.33 (s, 24H), 1.72 (s, 60H, Cp*). ^{31}P NMR (acetonitrile-d_3, 283 MHz) δ: 86.2 ($\nu_{1/2}$ = 850 Hz). UV−vis (THF): λ_{max} (ε) 373 nm (48,000 $M^{-1}cm^{-1}$). Experimental (calcd for $C_{170}H_{194}Co_8Cu_3LiN_6O_4P_6Se_8$) Co 10.19 (12.18) Se 16.43 (16.32) P 4.74 (4.80).

Synthesis of 1-Cu$_3$. Inside the glove box, [Li(thf)$_4$][**1**-Cu$_3$] (1.500 g, 0.47 mmol) is weighed out into a 100 mL Schlenk flask and dissolved in dichloromethane (35 mL). Tris(4-bromophenyl)-ammoniumyl hexachloroantimonate (0.400 g, 0.49 mmol) is weighed out into a vial and dissolved in tetrahydrofuran (10 mL). The solution is then added to the reaction mixture, which is left to stir at room temperature for 1 h. The reaction mixture is brought to constant mass under reduced pressure, redissolved in dichloromethane, and brought to constant mass again, to remove residual tetrahydrofuran. The residue is redissolved in dichloromethane, and the resulting solution filtered through a Celite plug. The volatiles are removed from the filtrate under reduced pressure. The residue is redissolved in tetrahydrofuran, layered with diethyl ether, and kept at room temperature overnight. The resulting precipitate is isolated via vacuum filtration through a medium-pore frit (0.596 g, 0.204 mmol, 44%). ^{1}H NMR (dichloromethane-d_2, 500 MHz) δ: 9.23 (d, 12H, -Ph), 9.02 (t, 6H, -Ph), 7.78 (t, 6H, -Ph), 7.18 (d, 12H, -Ph), 6.81 (d, 24H -Ph), 5.96 (d, 12H -C$_6H_4$-p-Me), 5.35, (t, 12H, -Ph), 2.64 (s, 18H, -Me). ^{31}P NMR (dichloromethane-d_2, 283 MHz) δ: −1159.92 ($\nu_{1/2}$ = 1200 Hz). ^{13}C NMR (dichloromethane-d_2, 126 MHz) δ 135.30, 133.93, 133.06, 132.32, 131.98, 130.69, 129.23, 126.38, 123.14, 121.42, 112.19, 19.38. μ_{eff} (Evan's method, CD_2Cl_2, 298 K): 1.68 μ_B. UV−vis (THF): λ_{max} (ε) 390 nm (38,000 $M^{-1}cm^{-1}$). Elemental analysis (ICP−MS): experimental (calculated for $C_{114}H_{102}Co_6Cu_3N_6P_6Se_8$) Co 12.47 (12.11) Se 21.25 (21.65) P 6.27 (6.37).

Synthesis of [Li(thf)$_4$]$_2$[1-Cu$_3$]. Inside the glove box, a 100 mL Schlenk flask with a Teflon-coated stir bar was charged with **1**-Li$_6$(py)$_6$ (2.440 g, 0.75 mmol) and copper(I) bromide dimethylsulfide (0.480 g, 2.33 mmol). Toluene (70 mL) and tetrahydrofuran (25 mL) are added to the flask, resulting in a dark brown solution upon mixing. After stirring the reaction mixture at 25 °C for 16 h, the resulting slurry is filtered through a medium-pore frit, and the solids on the frit are washed with toluene (20 mL), diethyl ether (50 mL), and pentane (50 mL). After collecting the solids and removing residual volatiles under vacuum, the product is obtained as a fine brown powder (1.660 g, 0.516 mmol, 64%). The spectroscopic data match that of the product synthesized by one-electron reduction of [Li(thf)$_4$][**1**-Cu$_3$] (see S1.2). Elemental analysis (ICP−MS): experimental (calculated for $C_{146}H_{166}Co_6Cu_3Li_2N_6O_8P_6Se_8$) Co 10.39 (10.07) Se 17.70 (18.00) P 5.05 (5.30).

■ ASSOCIATED CONTENT

Supporting Information

The Supporting Information is available free of charge at https://pubs.acs.org/doi/10.1021/acs.inorgchem.4c02639.

Experimental procedures and characterization data (PDF)

Optimized coordinates (XYZ)

Accession Codes

CCDC 2351182−2351185 contain the supplementary crystallographic data for this paper. These data can be obtained free of charge via www.ccdc.cam.ac.uk/data_request/cif, or by emailing data_request@ccdc.cam.ac.uk, or by contacting The Cambridge Crystallographic Data Centre, 12 Union Road, Cambridge CB2 1EZ, U.K.; fax: +44 1223 336033.

■ AUTHOR INFORMATION

Corresponding Author

Alexandra Velian − *Department of Chemistry, University of Washington, Seattle, Washington 98195, United States;* orcid.org/0000-0002-6782-7139; Email: avelian@uw.edu

Authors

Sebastian M. Krajewski − *Department of Chemistry, University of Washington, Seattle, Washington 98195, United States;* orcid.org/0000-0002-9755-2375

Robert J. Love, Jr. − *Department of Chemistry, University of Washington, Seattle, Washington 98195, United States*

Jonathan A. Kephart − *Department of Chemistry, University of Washington, Seattle, Washington 98195, United States;* orcid.org/0000-0003-4608-1160

Andrew C. Boggiano − *School of Chemistry and Biochemistry, Georgia Institute of Technology, Atlanta, Georgia 30332-0400, United States;* orcid.org/0000-0002-5444-485X

Henry S. La Pierre − *School of Chemistry and Biochemistry and Nuclear and Radiological Engineering and Medical Physics Program, School of Mechanical Engineering, Georgia Institute of Technology, Atlanta, Georgia 30332-0400, United States;* orcid.org/0000-0002-0895-0655

Werner Kaminsky − *Department of Chemistry, University of Washington, Seattle, Washington 98195, United States;* orcid.org/0000-0002-9100-4909

Complete contact information is available at: https://pubs.acs.org/10.1021/acs.inorgchem.4c02639

Notes

The authors declare no competing financial interest.

■ ACKNOWLEDGMENTS

This work was supported by the National Science Foundation (NSF) through a Faculty Early Career Development Program Award (1944843) and by the Research Corporation for Science Advancement through a Cottrell Scholars Award. The X-ray crystallography facility was funded through NSF Grant 0840520. The NMR spectroscopy facility was funded through NIH Grant S10 OD030224-01A1. S.M.K. thanks the Seattle ARCS Foundation and the Clean Energy Institute for funding. Use of the Stanford Synchrotron Radiation Lightsource (SSRL), SLAC National Accelerator Laboratory, is supported by the U.S. Department of Energy, Office of Science, Office of Basic Energy Sciences under Contract No. DE-AC02-76SF00515. The SSRL Structural Molecular Biology Program is supported by the DOE Office of Biological and Environmental Research, and by the National Institutes of Health, the National Institute of General Medical Sciences (including P30GM133894). A.C.B. and H.S.L. were supported by the NSF through a Faculty Early Career Development Program Award (1943452). The authors thank Ashley Weiland and Bruker AXS for their assistance with the crystallography of **1**-Cu_3, and Haruko Tateyama for assistance in preparing XANES samples.

■ REFERENCES

(1) Tedstone, A. A.; Lewis, D. J.; O'Brien, P. Synthesis, Properties, and Applications of Transition Metal-Doped Layered Transition Metal Dichalcogenides. *Chem. Mater.* **2016**, *28* (7), 1965−1974.

(2) Morales-Guio, C. G.; Hu, X. Amorphous Molybdenum Sulfides as Hydrogen Evolution Catalysts. *Acc. Chem. Res.* **2014**, *47* (8), 2671−2681.

(3) Chianelli, R. R.; Berhault, G.; Torres, B. Unsupported Transition Metal Sulfide Catalysts: 100 Years of Science and Application. *Catal. Today* **2009**, *147* (3), 275−286.

(4) Kibsgaard, J.; Tuxen, A.; Knudsen, K. G.; Brorson, M.; Topsøe, H.; Lægsgaard, E.; Lauritsen, J. V.; Besenbacher, F. Comparative Atomic-Scale Analysis of Promotional Effects by Late 3d-Transition Metals in MoS2 Hydrotreating Catalysts. *J. Catal.* **2010**, *272* (2), 195−203.

(5) Harris, S.; Chianelli, R. R. Catalysis by Transition Metal Sulfides: A Theoretical and Experimental Study of the Relation between the Synergic Systems and the Binary Transition Metal Sulfides. *J. Catal.* **1986**, *98* (1), 17−31.

(6) Muetterties, E. L.; Rhodin, T. N.; Band, E.; Brucker, C. F.; Pretzer, W. R. Clusters and Surfaces. *Chem. Rev.* **1979**, *79* (2), 91−137.

(7) Kibsgaard, J.; Jaramillo, T. F.; Besenbacher, F. Building an Appropriate Active-Site Motif into a Hydrogen-Evolution Catalyst with Thiomolybdate [Mo3S13]2−Clusters. *Nat. Chem.* **2014**, *6* (3), 248−253.

(8) Kephart, J. A.; Mitchell, B. S.; Chirila, A.; Anderton, K. J.; Rogers, D.; Kaminsky, W.; Velian, A. Atomically Defined Nanopropeller Fe3Co6Se8(Ph2PNTol)6: Functional Model for the Electronic Metal−Support Interaction Effect and High Catalytic Activity for Carbodiimide Formation. *J. Am. Chem. Soc.* **2019**, *141* (50), 19605−19610.

(9) Eaton, M. C.; Catalano, V. J.; Shearer, J.; Murray, L. J. Dinitrogen Insertion and Cleavage by a Metal−Metal Bonded Tricobalt(I) Cluster. *J. Am. Chem. Soc.* **2021**, *143* (15), 5649−5653.

(10) Mitchell, B. S.; Chirila, A.; Kephart, J. A.; Boggiano, A. C.; Krajewski, S. M.; Rogers, D.; Kaminsky, W.; Velian, A. Metal−Support Interactions in Molecular Single-Site Cluster Catalysts. *J. Am. Chem. Soc.* **2022**, *144* (40), 18459−18469.

(11) Amtawong, J.; Nguyen, A. I.; Tilley, T. D. Mechanistic Aspects of Cobalt−Oxo Cubane Clusters in Oxidation Chemistry. *J. Am. Chem. Soc.* **2022**, *144* (4), 1475−1492.

(12) Jin, R.; Liu, X.; Zhao, S.; Xing, Y.; Jin, R. Shape Effect of Atomically Precise Au25 Nanoclusters on Catalytic CO Oxidation. *J. Phys. Chem. C* **2022**, *126* (40), 17114−17122.

(13) Touchton, A. J.; Wu, G.; Hayton, T. W. [$Ni_{30}S_{16}(PEt_3)_{11}$]: An Open-Shell Nickel Sulfide Nanocluster with a "Metal-like" Core. *Chem. Sci.* **2022**, *13* (18), 5171−5175.

(14) Cesari, C.; Shon, J.-H.; Zacchini, S.; Berben, L. A. Metal Carbonyl Clusters of Groups 8−10: Synthesis and Catalysis. *Chem. Soc. Rev.* **2021**, *50* (17), 9503−9539.

(15) Beamer, A. W.; Buss, J. A. Synthesis, Structural Characterization, and CO_2 Reactivity of a Constitutionally Analogous Series of Tricopper Mono-, Di-, and Trihydrides. *J. Am. Chem. Soc.* **2023**, *145* (23), 12911−12919.

(16) Cooney, S. E.; Walls, M. R. A.; Schreiber, E.; Brennessel, W. W.; Matson, E. M. Heterometal Dopant Changes the Mechanism of Proton-Coupled Electron Transfer at the Polyoxovanadate-Alkoxide Surface. *J. Am. Chem. Soc.* **2024**, *146* (4), 2364−2369.

(17) Mondal, S.; Zhang, W.; Zhang, S. Thermodynamics of Proton-Coupled Electron Transfer at Tricopper μ-Oxo/Hydroxo/Aqua Complexes. *J. Am. Chem. Soc.* **2024**, *146* (22), 15036−15044.

(18) Lauritsen, J. V.; Kibsgaard, J.; Olesen, G. H.; Moses, P. G.; Hinnemann, B.; Helveg, S.; Nørskov, J. K.; Clausen, B. S.; Topsøe, H.; Lægsgaard, E.; Besenbacher, F. Location and Coordination of Promoter Atoms in Co- and Ni-Promoted MoS2-Based Hydrotreating Catalysts. *J. Catal.* **2007**, *249* (2), 220−233.

(19) Arnanz, A.; Marcos, M.-L.; Delgado, S.; González-Velasco, J.; Moreno, C. Electronic Communication through a Poly-Yne Carbonyldicobalt Complex Containing an Open Linear Triosmium Cluster. *Dalt Trans* **2009**, *1*, 168−176.

(20) Kephart, J. A.; Romero, C. G.; Tseng, C.-C.; Anderton, K. J.; Yankowitz, M.; Kaminsky, W.; Velian, A. Hierarchical Nanosheets Built from Superatomic Clusters: Properties, Exfoliation and Single-Crystal-to-Single-Crystal Intercalation. *Chem. Sci.* **2020**, *11* (39), 10744−10751.

(21) Kephart, J. A.; Boggiano, A. C.; Kaminsky, W.; Velian, A. Inorganic Clusters as Metalloligands: Ligand Effects on the Synthesis and Properties of Ternary Nanopropeller Clusters. *Dalton Trans.* **2020**, *49* (45), 16464−16473.

(22) Mitchell, B. S.; Kaminsky, W.; Velian, A. Tuning the Electronic Structure of Atomically Precise Sn/Co/Se Nanoclusters via Redox Matching of Tin(IV) Surface Sites. *Inorg. Chem.* **2021**, *60* (9), 6135−6139.

(23) Kephart, J. A.; Mitchell, B. S.; Kaminsky, W.; Velian, A. Multi-Active Site Dynamics on a Molecular Cr/Co/Se Cluster Catalyst. *J. Am. Chem. Soc.* **2022**, *144* (21), 9206−9211.

(24) Mitchell, B. S.; Krajewski, S. M.; Kephart, J. A.; Rogers, D.; Kaminsky, W.; Velian, A. Redox-Switchable Allosteric Effects in Molecular Clusters. *JACS Au* **2022**, *2* (1), 92−96.

(25) Kephart, J. A.; Zhou, D. Y.; Sandwisch, J.; Cajiao, N.; Krajewski, S. M.; Malinowski, P.; Chu, J.-H.; Neidig, M. L.; Kaminsky, W.; Velian, A. Caught in the Act of Substitution: Interadsorbate Effects on an Atomically Precise Fe/Co/Se Nanocluster. *ACS Cent. Sci.* **2024**, *10*, 1276.

(26) Johnson, B. J.; Antholine, W. E.; Lindeman, S. V.; Graham, M. J.; Mankad, N. P. A One-Hole Cu_4S Cluster with N_2O Reductase Activity: A Structural and Functional Model for Cu_Z*. *J. Am. Chem. Soc.* **2016**, *138* (40), 13107−13110.

(27) Arnett, C. H.; Chalkley, M. J.; Agapie, T. A Thermodynamic Model for Redox-Dependent Binding of Carbon Monoxide at Site-Differentiated, High Spin Iron Clusters. *J. Am. Chem. Soc.* **2018**, *140* (16), 5569−5578.

(28) Kim, Y.; Sridharan, A.; Suess, D. L. M. The Elusive Mononitrosylated [Fe4S4] Cluster in Three Redox States. *Angew. Chem., Int. Ed.* **2022**, *61* (47), No. e202213032.

(29) Ghebreamlak, S.; Stoian, S. A.; Lees, N. S.; Cronin, B.; Smith, F.; Ross, M. O.; Telser, J.; Hoffman, B. M.; Duin, E. C. The Active-

Site [4Fe-4S] Cluster in the Isoprenoid Biosynthesis Enzyme IspH Adopts Unexpected Redox States during Ligand Binding and Catalysis. *J. Am. Chem. Soc.* **2024**, *146* (6), 3926−3942.
(30) Juda, C. E.; Handford, R. C.; Bartholomew, A. K.; Powers, T. M.; Gu, N. X.; Meyer, E.; Roth, N.; Chen, Y.; Zheng, S.-L.; Betley, T. A. Cluster Dynamics of Heterometallic Trinuclear Clusters during Ligand Substitution, Redox Chemistry, and Group Transfer Processes. *Chem. Sci.* **2024**, *15* (21), 8242−8248.
(31) Mitchell, B. S.; Chirila, A.; Anderton, K. J.; Kaminsky, W.; Velian, A. Probing Edge/Support Electronic Cooperativity in Single Edge Fe/Co6Se8 Clusters. *Inorg. Chem.* **2023**, *62* (26), 10497−10503.
(32) Evangelio, E.; Ruiz-Molina, D. Valence Tautomerism: New Challenges for Electroactive Ligands. *Eur. J. Inorg. Chem.* **2005**, *2005* (15), 2957−2971.
(33) Kundu, N.; Maity, M.; Chatterjee, P. B.; Teat, S. J.; Endo, A.; Chaudhury, M. Reporting a Unique Example of Electronic Bistability Observed in the Form of Valence Tautomerism with a Copper(II) Helicate of a Redox-Active Nitrogenous Heterocyclic Ligand. *J. Am. Chem. Soc.* **2011**, *133* (50), 20104−20107.
(34) Lonnon, D. G.; Lee, S. T.; Colbran, S. B. Valence Tautomerism and Coordinative Lability in Copper(II)−Imidazolyl−Semiquinonate Anion Radical Models for the CuB Center in Cytochrome c Oxidases. *J. Am. Chem. Soc.* **2007**, *129* (18), 5800−5801.
(35) O'Brien, E. S.; Trinh, M. T.; Kann, R. L.; Chen, J.; Elbaz, G. A.; Masurkar, A.; Atallah, T. L.; Paley, M. V.; Patel, N.; Paley, D. W.; Kymissis, I.; Crowther, A. C.; Millis, A. J.; Reichman, D. R.; Zhu, X.-Y.; Roy, X. Single-Crystal-to-Single-Crystal Intercalation of a Low-Bandgap Superatomic Crystal. *Nat. Chem.* **2017**, *9* (12), 1170−1174.
(36) Banthia, S.; Samanta, A. Synthesis and Structure of Unusually Stable Linear Copper(I) Complexes with Blue Fluorescence. *Polyhedron* **2006**, *25* (11), 2269−2276.
(37) Zhang, Q.; Wilson, P.; Li, Z.; McHale, R.; Godfrey, J.; Anastasaki, A.; Waldron, C.; Haddleton, D. M. Aqueous Copper-Mediated Living Polymerization: Exploiting Rapid Disproportionation of CuBr with Me6TREN. *J. Am. Chem. Soc.* **2013**, *135* (19), 7355−7363.
(38) Connelly, N. G.; Geiger, W. E. Chemical Redox Agents for Organometallic Chemistry. *Chem. Rev.* **1996**, *96* (2), 877−910.
(39) Le Clainche, L.; Giorgi, M.; Reinaud, O. Synthesis and Characterization of a Novel Calix[4]Arene-Based Two-Coordinate Copper(I) Complex That Is Unusually Resistant to Dioxygen. *Eur. J. Inorg. Chem.* **2000**, *2000* (9), 1931−1933.
(40) Sanyal, I.; Karlin, K. D.; Strange, R. W.; Blackburn, N. J. Chemistry and Structural Studies on the Dioxygen-Binding Copper-1,2-Dimethylimidazole System. *J. Am. Chem. Soc.* **1993**, *115* (24), 11259−11270.
(41) Sorrell, T. N.; Jameson, D. L. Synthesis, Structure, and Reactivity of Monomeric Two-Coordinate Copper(I) Complexes. *J. Am. Chem. Soc.* **1983**, *105* (19), 6013−6018.
(42) A Search for All Cu···N Bond Lengths in the Cambridge Structural Database (April 2024) Yielded 212141 Hits between 1.147 and 3.037 Å (Mean 2.0(1) Å).; 2024.
(43) Xu, Y.; Chen, J.; Aydt, A. P.; Zhang, L.; Sergeyev, I.; Keeler, E. G.; Choi, B.; He, S.; Reichman, D. R.; Friesner, R. A.; Nuckolls, C.; Steigerwald, M. L.; Roy, X.; McDermott, A. E. Electron and Spin Delocalization in [Co6Se8(PEt3)6]0/+1 Superatoms. *ChemPhysChem* **2024**, *25* (2), No. e202300064.
(44) Wagner, C. L.; Tao, L.; Thompson, E. J.; Stich, T. A.; Guo, J.; Fettinger, J. C.; Berben, L. A.; Britt, R. D.; Nagase, S.; Power, P. P. Dispersion-Force-Assisted Disproportionation: A Stable Two-Coordinate Copper(II) Complex. *Angew. Chem., Int. Ed.* **2016**, *55* (35), 10444−10447.
(45) Wagner, C. L.; Tao, L.; Fettinger, J. C.; Britt, R. D.; Power, P. P. Two-Coordinate, Late First-Row Transition Metal Amido Derivatives of the Bulky Ligand -N(SiPri3)Dipp (Dipp = 2,6-Diisopropylphenyl): Effects of the Ligand on the Stability of Two-Coordinate Copper(II) Complexes. *Inorg. Chem.* **2019**, *58* (13), 8793−8799.
(46) James, A. M.; Laxman, R. K.; Fronczek, F. R.; Maverick, A. W. Phosphorescence and Structure of a Tetrameric Copper(I)−Amide Cluster. *Inorg. Chem.* **1998**, *37* (15), 3785−3791.
(47) A Search for All Cu···Se Bond Lengths in the Cambridge Structural Database (March 2024) Yielded 4798 Hits between 2.163 and 3.170 Å (Mean 2.5(1) Å).; 2024.
(48) Hughbanks, T.; Hoffmann, R. Molybdenum Chalcogenides: Clusters, Chains, and Extended Solids. The Approach to Bonding in Three Dimensions. *J. Am. Chem. Soc.* **1983**, *105* (5), 1150−1162.
(49) Choi, B.; Yu, J.; Paley, D. W.; Trinh, M. T.; Paley, M. V.; Karch, J. M.; Crowther, A. C.; Lee, C.-H.; Lalancette, R. A.; Zhu, X.; Kim, P.; Steigerwald, M. L.; Nuckolls, C.; Roy, X. Van Der Waals Solids from Self-Assembled Nanoscale Building Blocks. *Nano Lett.* **2016**, *16* (2), 1445−1449.
(50) A Search for All Co···Co Bond Lengths in the Cambridge Structural Database (March 2024) Yielded 8297 Hits between 1.978 and 3.219 Å (Mean 2.5(2) Å).; 2024.
(51) Bridgeman, A. J.; Cavigliasso, G.; Ireland, L. R.; Rothery, J. The Mayer Bond Order as a Tool in Inorganic Chemistry. *J. Chem. Soc., Dalton Trans.* **2001**, *14*, 2095−2108.
(52) Hernández Sánchez, R.; Champsaur, A. M.; Choi, B.; Wang, S. G.; Bu, W.; Roy, X.; Chen, Y.-S.; Steigerwald, M. L.; Nuckolls, C.; Paley, D. W. Electron Cartography in Clusters. *Angew. Chem., Int. Ed.* **2018**, *57* (42), 13815−13820.
(53) Zhu, Y.; Guo, J.; Qiu, X.; Zhao, S.; Tang, Z. Optical Activity of Chiral Metal Nanoclusters. *Acc. Mater. Res.* **2021**, *2* (1), 21−35.
(54) Pérez-García, L.; Amabilino, D. B. Spontaneous Resolution under Supramolecular Control. *Chem. Soc. Rev.* **2002**, *31* (6), 342−356.
(55) Evans, D. F. 400. The Determination of the Paramagnetic Susceptibility of Substances in Solution by Nuclear Magnetic Resonance. *J. Chem. Soc. Resumed* **1959**, 2003−2005.
(56) Köhler, F. H.. *Paramagnetic Complexes in Solution: The NMR Approach*. In Encyclopedia of Magnetic Resonance; John Wiley & Sons, Ltd: Chichester, U.K., 2011.
(57) Mugiraneza, S.; Hallas, A. M. Tutorial: A Beginner's Guide to Interpreting Magnetic Susceptibility Data with the Curie-Weiss Law. *Commun. Phys.* **2022**, *5* (1), 1−12.
(58) Wilcke, S. L.; Lee, Y.-J.; Cairns, E. J.; Reimer, J. A. Covalency Measurements via NMR in Lithium Metal Phosphates. *Appl. Magn. Reson.* **2007**, *32* (4), 547−563.
(59) Palstra, T. T. M.; Steigerwald, M. L.; Ramirez, A. P.; Kwon, Y.-U.; Stuczynski, S. M.; Schneemeyer, L. F.; Waszczak, J. V.; Zaanen, J. Electron Correlations on a Mesoscopic Scale: Magnetic Properties of Transition Metal Telluride Cluster Compounds. *Phys. Rev. Lett.* **1993**, *71* (11), 1768−1771.
(60) Van Vleck, J. H.; Frank, A. The Effect of Second Order Zeeman Terms on Magnetic Susceptibilities in the Rare Earth and Iron Groups. *Phys. Rev.* **1929**, *34* (11), 1494−1496.
(61) Aleshin, D. Y.; Nikovskiy, I.; Novikov, V. V.; Polezhaev, A. V.; Melnikova, E. K.; Nelyubina, Y. V. Room-Temperature Spin Crossover in a Solution of Iron(II) Complexes with N,N′-Disubstituted Bis(Pyrazol-3-Yl)Pyridines. *ACS Omega* **2021**, *6* (48), 33111−33121.
(62) Perryman, J. T.; Hyler, F. P.; Ortiz-Rodríguez, J. C.; Mehta, A.; Kulkarni, A. R.; Velázquez, J. M. X-Ray Absorption Spectroscopy Study of the Electronic Structure and Local Coordination of 1st Row Transition Metal-Promoted Chevrel-Phase Sulfides. *J. Coord. Chem.* **2019**, *72*, 1322.
(63) Hyler, F. P.; Bille, B. A. W.; Ortíz-Rodríguez, J. C.; Sanz-Matias, A.; Roychoudhury, S.; Perryman, J. T.; Patridge, C. J.; Singstock, N. R.; Musgrave, C. B.; Prendergast, D.; Velázquez, J. M. X-Ray Absorption Spectroscopy Insights on the Structure Anisotropy and Charge Transfer in Chevrel Phase Chalcogenides. *Phys. Chem. Chem. Phys.* **2022**, *24* (28), 17289−17294.
(64) Kompch, A.; Sahu, A.; Notthoff, C.; Ott, F.; Norris, D. J.; Winterer, M. Localization of Ag Dopant Atoms in CdSe Nanocrystals by Reverse Monte Carlo Analysis of EXAFS Spectra. *J. Phys. Chem. C* **2015**, *119* (32), 18762−18772.

https://doi.org/10.1021/acs.inorgchem.4c02639
Inorg. Chem. 2024, 63, 20388−20397

(65) Yao, S. A.; Lancaster, K. M.; Götz, A. W.; DeBeer, S.; Berry, J. F. X-Ray Absorption Spectroscopic, Crystallographic, Theoretical (DFT) and Chemical Evidence for a Chalcogen−Chalcogen Two-Center/Three-Electron Half Bond in an Unprecedented "Subselenide" Se23−Ligand. *Chem.—Eur. J.* **2012**, *18* (30), 9179−9183.
(66) Henthorn, J. T.; DeBeer, S. Selenium Valence-to-Core X-Ray Emission Spectroscopy and Kβ HERFD X-Ray Absorption Spectroscopy as Complementary Probes of Chemical and Electronic Structure. *Inorg. Chem.* **2022**, *61* (6), 2760−2767.
(67) Lu, T.; Chen, F. Multiwfn: A Multifunctional Wavefunction Analyzer. *J. Comput. Chem.* **2012**, *33* (5), 580−592.
(68) Reber, A. C.; Chauhan, V.; Khanna, S. N. Symmetry and Magnetism in Ni9Te6 Clusters Ligated by CO or Phosphine Ligands. *J. Chem. Phys.* **2017**, *146* (2), No. 024302.
(69) Frisch, M. J.; Trucks, G. W.; Schlegel, H. B.; Scuseria, G. E.; Robb, M. A.; Cheeseman, J. R.; Scalmani, G.; Barone, V.; Petersson, G. A.; Nakatsuji, H.; Li, X.; Caricato, M.; Marenich, A. V.; Bloino, J.; Janesko, B. G.; Gomperts, R.; Mennucci, B.; Hratchian, H. P.; Ortiz, J. V.; Izmaylov, A. F.; Sonnenberg, J. L.; Williams; Ding, F.; Lipparini, F.; Egidi, F.; Goings, J.; Peng, B.; Petrone, A.; Henderson, T.; Ranasinghe, D.; Zakrzewski, V. G.; Gao, J.; Rega, N.; Zheng, G.; Liang, W.; Hada, M.; Ehara, M.; Toyota, K.; Fukuda, R.; Hasegawa, J.; Ishida, M.; Nakajima, T.; Honda, Y.; Kitao, O.; Nakai, H.; Vreven, T.; Throssell, K.; Montgomery, Jr., J. A.; Peralta, J. E.; Ogliaro, F.; Bearpark, M. J.; Heyd, J. J.; Brothers, E. N.; Kudin, K. N.; Staroverov, V. N.; Keith, T. A.; Kobayashi, R.; Normand, J.; Raghavachari, K.; Rendell, A. P.; Burant, J. C.; Iyengar, S. S.; Tomasi, J.; Cossi, M.; Millam, J. M.; Klene, M.; Adamo, C.; Cammi, R.; Ochterski, J. W.; Martin, R. L.; Morokuma, K.; Farkas, O.; Foresman, J. B.; Fox, D. J. *Gaussian 16 Rev. C.01*, 2016.

https://doi.org/10.1021/acs.inorgchem.4c02639
Inorg. Chem. 2024, 63, 20388−20397